New Nanosized (Gd3+, Sm3+) Co-doped Zinc Ferrite for Telecommunication Applications. Magnetic and Structural Properties.

yassine belaiche (yassine.belaiche@um5s.net.ma)
Universite Mohammed V de Rabat Faculte des Sciences
K. Minaoui
Universite Mohammed V de Rabat
Mohamed Ouadou
Universite Mohammed V de Rabat
MMoustapha Elansary
Universite Mohammed V de Rabat

Research Article

Keywords: thermogravimetric, nanocrystalline ferrite

Posted Date: August 18th, 2020

DOI: https://doi.org/10.21203/rs.3.rs-61215/v1

New Nanosized (Gd^{3+}, Sm^{3+}) Co-doped Zinc Ferrite for Telecommunication Applications. Magnetic and Structural Properties.

Y. Belaiche [a], K. Minaoui [a], M. Ouadou [a], M. Elansary [b]

a. LRIT Laboratory, associated unit to CNRST (URAC29), IT Rabat Center, Faculty of Sciences in Rabat, Mohammed V University, Rabat, Morocco.

b. Nanomaterials and Nanotechnology Unit, E.N.S. Energy Research Centre. Mohammed V University, B.P. 5118 Takaddoum, Rabat, Morocco.

Abstract

Highly crystalline $ZnFe_{1.98}Sm_{0.01}Gd_{0.01}O_4$ nanoferrites were prepared by co-precipitation method for the first time. The nanoparticles were characterized using thermogravimetric and differential scanning calorimetry analysis (TGA and DSC), which shows the thermal behavior of the reagents mixture. XRD analysis confirms the formation of nanocrystalline ferrite phase with $Fd\bar{3}m$ space group, and the particle size was observed to be 11 nm . The FTIR reveals two based bands of absorption characterize the formation of the spinel structure. An exhaustive study of the magnetic properties, morphology, crystallinity and effects of co-doping Gd^{3+} and Sm^{3+} was presented in detail. The average crystallites size was observed to decrease for Gd^{3+} and Sm^{3+} co-doping. Magnetic measurements reveal weak ferrimagnetic behavior at low temperature and superparamagnetic at high temperature with a blocking temperature at 55 K.

1. Introduction

In recent years, nanotechnology has metamorphosed into a global technology, playing a crucial role not only in materials science, but also in several areas such as telecommunications and information technology, microelectronics, electronics and others. Nanoscience's are developing at an extraordinarily fast pace and rapid progress is being made in this field. With the advent of nanoscience's and nanotechnologies, new devices are appearing and thanks to nanotechnologies, obsolete devices are being replaced. Quantum mechanics has permitted a vertiginous understanding of physical and electronic properties at the nanometric scale, so physicists are naturally taking the lead in exploiting this brand new field of science for the benefit of human development. Magnetism, or more particularly nanomagnetic materials, will

certainly play a crucial role in the implementation of new and more sophisticated applications using nanotechnologies. It should be noted that with magnetism and nanotechnology, devices based on new properties and functionalities will ineluctably emerge. The nanoferrite have been used in wide technological applications such as, nano-antennae, radio frequency circuits, transformer cores and read and write heads for high speed digital tapes. Thus, good control of the theoretical formalism of the role of magnetism and magnetic material properties in telecommunication systems and devices, is a great challenge for the advancement of device design and performance. Nanoferrites have been widely studied and applied in antennas [1]–[4] , circulators [5]–[7], insulators [8]–[10] and inductors [11]–[14].

Due to their low power losses over a large range of frequencies, Zn-Mn ferrites are beneficial as the base materials for inductors and transformers[15] . Also important for spinel-structured Zn-Mg ferrites are their high resistivity, low Foucault currents, magnetic and dielectric losses [16] . One of the key parameters in determining the performance and applications of magnetic materials are dielectric and magnetic power losses. However, the main cause that influenced dielectric and magnetic power losses was the contribution of total losses such as current losses of Foucault, hysteresis and other losses [17], [18] . Zn-Ni ferrites are the best and most versatile ferrites and have been extensively studied because of their many applications such as transducers, filters, memory devices, sensors, transformers, loading coils, various electronic devices and resonators, high-frequency microwave applications and devices[19], [20]. These three versatile mixed ferrites allow a wide range of applications in the frequency range from low to very high microwave frequencies.

Interestingly, with the development of technology and miniaturization, research and development has focused on new antenna technology and new substrates, adaptive network configuration, dynamic structure, sustainable performance, low cost and energy efficient use, etc. $Zn_{0.8}Mn_{0.2}Fe_2O_4$ zinc-manganese ferrite with low loss properties (loss tangent 0<0.03) is used as an antenna substrate to introduce a new dielectric substrate for compact 5G antenna mounting [21]. Provided that the nanoferrites Zn-Mg, Zn-Mn and $MgSm_xGd_yFe_{2-x-y}O_4$ [22] , have given very good results, for the design of a micro-strip patch antenna, in the same sense our work will focus on $ZnFe_{1.98}Gd_{0.01}Sm_{0.01}O_4$.

It is well known that nanoferrite properties can be easily modified and optimized by integrating and properly adding divalent or trivalent cations into the spinel structure. To our knowledge and according to the literature, no published studies are available on the structure, morphology and magnetic properties of zinc ferrite co-doped by Gd^{3+} and Sm^{3+}. In the present

work, we report on the synthesis of $ZnFe_{1.98}(GdSm)_{0.01}O_4$ nanoparticles . The effect of doping on the structural, morphological, solubility and magnetic properties is studied in detail.

2. Characterization

The sample synthesized was characterized using The Thermal analysis was carried out in TGA (Q500-TAInstruments). The X-ray diffraction analyses were carried out to determine the single phase. Measurements were made by an X-ray diffractometer (PANalytical, PW3050/60, XRD). The lattice parameter and crystallite sizes were calculated by the Rietveld refinement method and Debye–Scherrer formula respectively. Fourier Transform-Infrared spectra (FT-IR) of the samples were realized using an ABB Bomem FTLA 2000-102 spectrometer. Transmission electron microscopy (TEM) Tecnai G2 microscope were used to determine the particle morphology. The magnetic measurements were carried by Magnetic Property Measurement System (Quantum Design MPMS-XL-7AC SQUID) for study the magnetic behavior.

3. Experimental details :

The nanoparticles $ZnFe_{1.98}Sm_{0.01}Gd_{0.01}O_4$ were prepared by the chemical co-precipitation method. Firstly, $Fe(NO_3)_3.9H_2O$ (≥ 98.0% pure, Sigma-Aldrich) , $Zn(NO_3)_2.6H_2O$ (≥ 99.0% pure, Sigma-Aldrich) , $Gd(NO_3)_2.6H_2O$ (≥ 99.0% pure, Alfa Aesar) and $Sm(NO_3)_2.6H_2O$ (≥ 99.0% pure, Alfa Aesar) were dissolved stoichiometrically in deionized water, the entire mixture was stirred with a magnetic stirrer until the all compounds are completely dissolved at a temperature of 60°C for 15min . The prepared solution was co-precipitated at pH value of 10.5 using (3M) of Sodium hydroxide (NaOH) with two drops of oleic acid. The solution obtained is mixed at 80 ° C for 1h 15min and then abandoned to precipitate. The separation of the precipitates from solutions was done by micro-filter paper and washed several times using deionized water and subsequently dried into an oven at 100 ℃. The powder obtained were calcined at 700°C for 2h.

4. Results and discussion

4.1.Thermal analysis

In order to study the formation process of $ZnFe_{1.98}Sm_{0.01}Gd_{0.01}O_4$ powders, TGA and DSC analyses are used to determine the decomposition process of precursors and surfactant. The TGA and DSC curves are shown in Figure 1. Thermal decomposition takes place in three different stages, as can be seen on the TGA curves. Fig. 1 reveals two ramps of mass loss around the temperature range (100–160°C), followed by a prolonged loss of mass from 180 to

560 °C due to the combustion of the residual organic components and nitrates. The first weight loss of ~ 6% corresponds to loss of adsorbed water molecules present in the samples. The second weight loss of ~ 3,8%, is due mainly to the decomposition of weakly bound functional group (–COOH) from oleic acid surfactant, and to which corresponds a strong endothermic peak in DSC. The total loss of weight corresponds to 9.8% of the starting weight. The TGA curve pattern is linear from 560 to 700°C and after it no more weight loss took place which reflects the formation of nanocrystalline spinel ferrite.

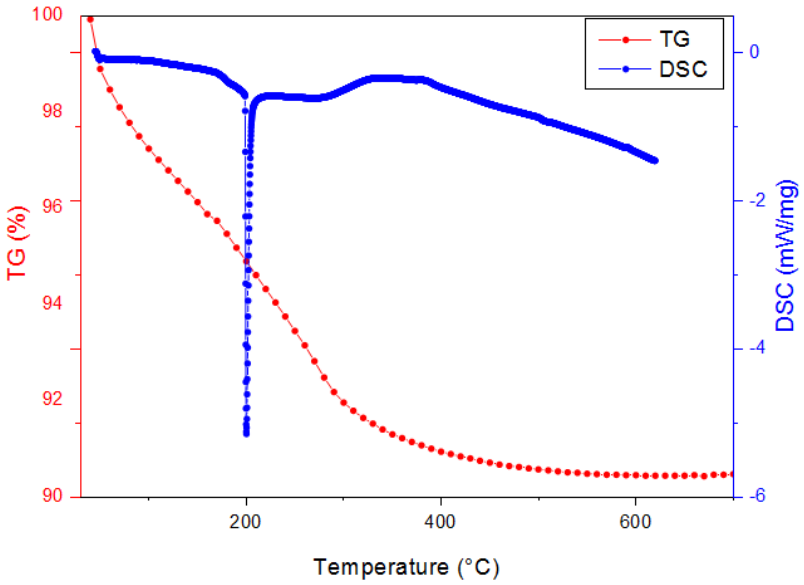

Fig.1: Thermal analysis of the polymeric and nitrate precursors

4.2.XRD Analysis

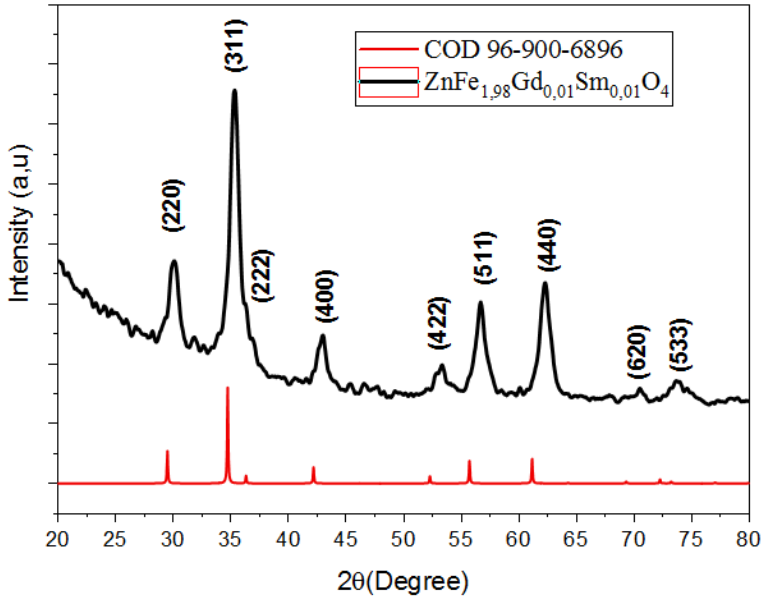

Fig.2. Patterns (XRD) of$ZnFe_{1.98}Gd_{0.01}Sm_{0.01}O_4$calcined at 700° C

The structural analysis of prepared sample has been carried out by powder XRD technique and the pattern is presented in figure 2. All the indexed peaks confirm the formation of single-phase normal spinel cubic structure with space group $Fd\bar{3}m$. There is no evidence of any other impurity or second phase in the XRD spectra. The reticular planes (220), (311), (222), (400), (422), (511), (440), (620) and (533) are corresponding to the diffraction peaks located at 2θ values of 30.10°, 35.31°, 36.05°, 43.00°, 53.36°, 56.71°, 62.32°, 70.54° and 73.68°

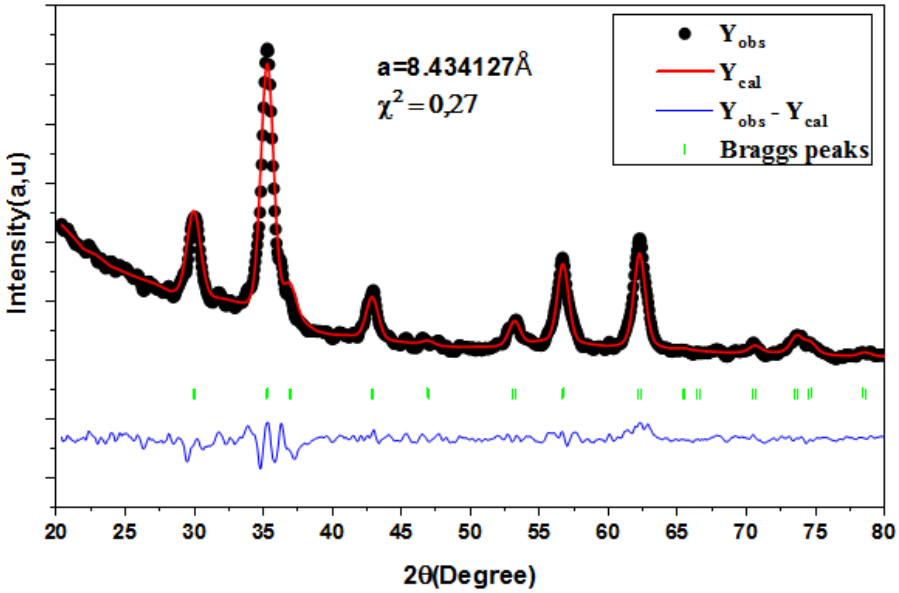

respectively, which exactly matched with COD data, card no #96-900-6896, for $ZnFe_2O_4$.

Fig.3. Rietveld refined XRD pattern for the $ZnFe_{1.98}Gd_{0.01}Sm_{0.01}O_4$ sample

To further reveal the detailed structural parameters, Rietveld refinement was carried out on XRD data of the sample using FullProf software, see Fig.3. The fit was determined by the quality of the fit as well as the low values of the reliable factors ($\chi^2 < 1$) **.** A very good fitting parameters is obtained by fitting the respective experimental data. All peaks have been indexed in the spinel structure with a space group $Fd\bar{3}m$ indicating the precision of the results. The obtained lattice parameter is **a = 8.4341** Å for $ZnFe_{1.98}Gd_{0.01}Sm_{0.01}O_4$ is in relatively good agreement with those found in the literature [23].

It is well known that the incorporation of rare earth elements in a spinel lattice can lead to a micro-strain of the lattice. In this case, the Williamson-Hall method was used to estimate the average size of the crystallites and the strain of the lattice. The average crystallite size D_{W-H} and the induced strain have been calculated using the W-H equation;

$$\beta \cos(\theta) = \frac{k\lambda}{D_{W-H}} + 4\varepsilon \sin(\theta)$$

where k is a constant and ε is the strain induced in the samples. The Williamson-Hall graphs reveal that for all prominent peaks and the best linear fit applied. Crystallite size was calculated from the intercept and lattice deformation was obtained from the slope of the linear function analysis [24]. The crystallite size and lattice micro-strain are given in Table 1.

As shown in the Table 1, The calculated value of average crystallites size (D), of samples co-doped with Gd^{3+} and Sm^{3+} ions is smaller than that of the undoped zinc ferrite $ZnFe_2O_4$ synthetized by Tatachuk et al [25], this is due to the fact that more energy is required to insert the RE = (Gd^{3+}, Sm^{3+}) ions, because the binding energy is a part of the internal energy. Indeed, RE^{3+} ions have an empty or half or full 4f electron shell with a stable structure, so that the sample containing the RE^{3+} ions has a high thermal stability. The bond strengths of Zn^{2+}-O^{2-} , Fe^{3+}-O^{2-}, Sm^{3+}-O^{2-} and Gd^{3+}-O^{2-} are 159 (kJ mol^{-1}), 390 (kJ mol^{-1}), 573 (kJ mol^{-1}) and 715 (kJ mol^{-1}), respectively. As a result, zinc ferrites co-doped Gd^{3+} and Sm^{3+} exhibit greater thermal stability than pure zinc ferrites. Samples of zinc ferrites co-doped Gd^{3+} and Sm^{3+} therefore require more energy to boost crystal growth. It should be noted that a typically similar behavior with respect to the different rare earth dopants has been reported in the literature[26], [27].

For micro-strain it is clear that the value of ε is negative as there is compression in the lattice [28]. this can be explained by the exchange interaction force in the system due to the presence of the doping elements Gd^{3+} and Sm^{3+} having a high magnetic moment of spin. The details of this compression will be discussed in the magnetic discussion section.

Theoretical density $\boldsymbol{\rho_{X-ray}}$ is calculate using the following relation:

$$\boldsymbol{\rho_{X-ray} = \frac{8M}{Na^3}} \quad (2)$$

where **M** is the molecular weight of the sample, **N** is the Avogadro's number and **a** is the lattice parameter.

The calculated value of the X-ray density of $ZnFe_{1.98}Gd_{0.01}Sm_{0.01}O_4$ is larger, this is due to the increase in the molecular weight of the sample by doping with Gd^{3+} and Sm^{3+}.

Sample	Lattice parameter (Å)	D_{W-H} (nm)	ε	Theoretical density (g/cm^3)	$u(\bar{4}3m)$ (Å)
$Zn Fe_{1.98}Sm_{0.01}Gd_{0.01}O$	8.4341	5	-0.00247	5.3813	0.3780

Table 1. lattice parameter (a), Crystallite size (D_{W-H}), ε micro-strain, x-ray density ($\boldsymbol{\rho_{X-ray}}$) and the oxygen position parameter u for $ZnFe_{1.98}Gd_{0.01}Sm_{0.01}O_4$ nanoparticles.

	Site A	**Site B**	**a_{exp}(Å)**	**r_A(Å)**	**r_B(Å)**	**a_{th}(Å)**	**Method**	**Ref**
Co-precipitation	**$Zn_{0.57}Fe_{0.43}$**	**$Zn_{0.43}Fe_{1.55}Sm_{0.01}Gd_{0.01}$**	**8.4341**	**0.7099**	**0.6878**	**8.2271**	**Mathematical model**	**Present work**
Sol-gel	**$Zn_{0.77}Fe_{0.23}$**	**$Zn_{0.23}Fe_{1.72}La_{0.05}$**	**8.465**	**0.7239**	**0.6870**	**8.2014**	**Rietveld refinement**	**[29]**
	$Zn_{0.596}Fe_{0.395}$	**$Zn_{0.404}Fe_{1.559}Gd_{0.046}$**	**8.478**	**0.7056**	**0.6933**	**8.2353**	**Rietveld refinement**	**[30]**
Conventional solid state	**$Zn_{0.89}Fe_{0.11}$**	**$Zn_{0.11}Fe_{1.89}$**	**8.44**	**0.7332**	**0.6738**	**8.2241**	**Mathematical model**	**[31]**
The microwave assisted combution	**$Zn_{0.98}Fe_{0.02}$**	**$Fe_{1.88}Gd_{0.1}Zn_{0.02}$**	**8.4366**	**0.7386**	**0.6842**	**8.2615**	**Rietveld refinement**	**[32]**

Table 2. The cationic distribution of zinc ferrite prepared by different methods found in the literature

Numerous studies on the effect of the substitution of a single rare earth element (RE) and transition metals on the physico-chemical properties of zinc ferrite have been carried out in the literature, introducing important structural modifications that lead to interesting physical properties. These modifications depend on the distribution of cations between the two

crystallographic sites A and B of spinel ferrites and their valence state.[33]–[36] . For spinel ferrites, cationic distribution at tetrahedral and octahedral sites plays an important role in the order to evaluate the electrical, morphological, chemical and physical properties. According to the literature it has been reported that bulk zinc ferrite has a normal spinel structure[37], however, this particularity disappears at the nanometer size and is replaced by a mixed spinel. [38] . The cationic distribution in $ZnFe_2O_4$ becomes $(Zn_{1-x}Fe_x)[Zn_xFe_{2-x}]O_4$ where parenthesis and square brackets denote, the cation sites of tetrahedral (A-sites) and octahedral [B-sites] respectively.

Knowing that we work at the nanometric scale and that we dope with rare earths Sm and Gd much larger than Zn and Fe, and taking into account the result of Kolekar et al. [39] which showed that the probability of rare earth ions occupying tetrahedral sites can be excluded, since these sites are too small to be occupied by large rare earth ions, hence the distribution of cations in this case can be written as follows :

$$\left[Zn_{(1-\delta)}Fe_{\delta}\right]^{A}\left[Zn_{\delta}Fe_{(1.98-\delta)}(SmGd)_{0.01}\right]^{B} \qquad (3)$$

Where δ is the degree of inversion, which reflects the percentage of Zn^{2+} and Fe^{3+} at the tetrahedral and octahedral sites. It is well known that the mean ionic radii of ions at tetrahedral site r_{tet} and octahedral site r_{oct}, in terms of their concentrations can be written as:

$$r_{tet} = [(1-\delta)r_{Zn^{2+}} + \delta r_{Fe^{3+}}] \qquad (4)$$

$$r_{oct} = \frac{1}{2}\left[\delta r_{Zn^{2+}} + (1.98-\delta)r_{Fe^{3+}} + 0{,}01(r_{Gd^{3+}} + r_{Sm^{3+}})\right] \qquad (5)$$

Where, $r_{Fe^{3+}}, r_{Zn^{2+}}, r_{Sm^{3+}} and\ r_{Gd^{3+}}$ are radius of Fe^{3+}, Zn^{2+}, Sm^{3+} and Gd^{3+} ions respectively.

The theoretical lattice parameter can be calculated theoretically by the following equation:

$$a_{th} = \frac{8}{3\sqrt{3}}\left[(r_A + R_O) + \sqrt{3}(r_B + R_O)\right] \qquad (6)$$

where R_O is the radius of oxygen ion ($R_O = 1.32$ Å), andr_A and r_B are the radii of the tetrahedral and octahedral sites, respectively.

The oxygen position parameter or the anionic parameter **u**, which is the distance between the oxygen ion and the face of the edge along the cube diagonal of the spinel lattice is calculated by [40]:

$$u(\bar{4}3m) = \frac{(r_A + R_0)}{a_{exp}\sqrt{3}} + \frac{1}{4} \quad (7)$$

(for the unit-cell origin at $\bar{4}3m$ on an A-site cation)

Where, r_A ionic radius of A-site, R_0 is ionic radius of oxygen ion.

Considering the proposed cationic distribution formula, a computer program has been developed to adjust and find a better agreement between the theoretical values and the experimental data, of the magnetic moment and the lattice constant, optimizing the value of the degree of inversion (δ) on the tetrahedral and octahedral sites. The reliability of the suggested cation distribution is validated by comparing the computed values and experimental data of the lattice parameter and magnetic moment, as shown in **Table 2.**

The theoretical values of a_{th}, r_A and r_B and u have been calculated from the proposed cation distribution and are listed in the table1. It can be seen that the value of r_A, r_B and a_{th} are comparable with values found in the literature as shown in **Table 1** . The value $u(\bar{4}3m)$ is slightly higher than that of the ideal oxygen parameter (u_{ideal}= 0.375Å), due to the deformation of the unit cells, as a result of which the A sites and B have expanded and contracted respectively, this phenomenon is the consequence of co-doping by Gd^{3+} and Sm^{3+}, which have large radii. As a consequence, Zn^{2+} and Fe^{3+} ions are distributed in both site A and B.

4.3. FTIR Spectrum

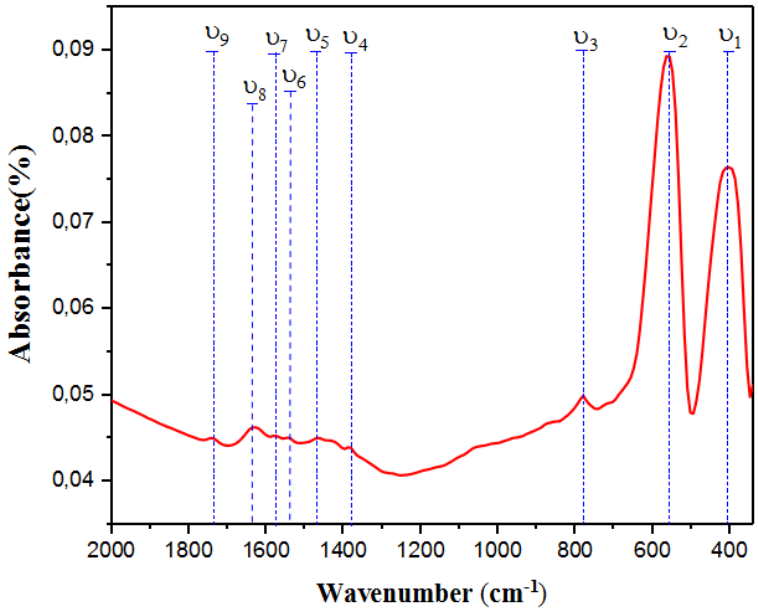

Fig.4. FTIR spectra of sample $ZnFe_{1.98}Gd_{0.01}Sm_{0.01}O_4$

To confirm the complete reaction and formation of the single ferrite phase after annealing. The FTIR spectra of the annealed ferrite sample was recorded in the range of 2000–350 cm^{-1} . **Fig.4** shows the FTIR spectra of sample.

In the FTIR spectra of spinel ferrites there are two main characteristic absorption peaks, which are related to intrinsic vibrations of oxygen bonds with metal cations at sites A and B[41].Where the first band is located at 408,87 cm^{-1} corresponds to the stretching vibrations of the M↔O bond at the octahedral site. And the second located at 563,17 cm^{-1} is attributed to the vibration of the M↔O bond at the tetrahedral site.

The absorption band located at 779,18 cm^{-1} and at 1138,09 cm^{-1} corresponds to the C–H stretching vibrations and the asymmetric vibrations of the C–O stretching vibrations respectively, while the absorption peaks in the range of 1400 and 1650 are assigned to C=C bending vibrations. The band absorption peak at 1735 cm^{-1} are attributable to the C=O stretching and bending vibrations. All bands in the range of 700-1750 cm^{-1} indicate the presence
of a small amount of oleic acid in the sample [42] as shown in **Table 3**.

	Wave number (cm^{-1})	Group
ν_1	408.87	Stretching vibration of (M_{octa} ↔O)
ν_2	563.17	Stretching vibration of (M_{tetra} ↔O)
ν_3	779.18	Stretching vibration of C-H
ν_4	1138.09	Stretching vibration of C-O
ν_5	1465.7	Stretching vibration of C=C
ν_6	1542.9	
ν_7	1627.8	
ν_8	1735.8	Stretching vibration of C=O

Table 3. Attribution of the vibration bands observed on the FT-IR spectra of $ZnFe_{1.98}(GdSm)_{0.01}O_4$ obtained by co-precipitation.

From the FTIR spectra, the results also showed that distortion occurs in the tetrahedral and octahedral sites after doping by Gd and Sm. The presence of the two characteristics peaks, and the absence of peaks associated to secondary phases or impurities, confirm the single phase formation of the investigated co-doped ferrites. These results are in perfect agreement with those determined by X-ray diffraction, which prove that a pure phase is obtained where Gd^{3+} and Sm^{3+} are totally soluble.

4.4. Morphological Study

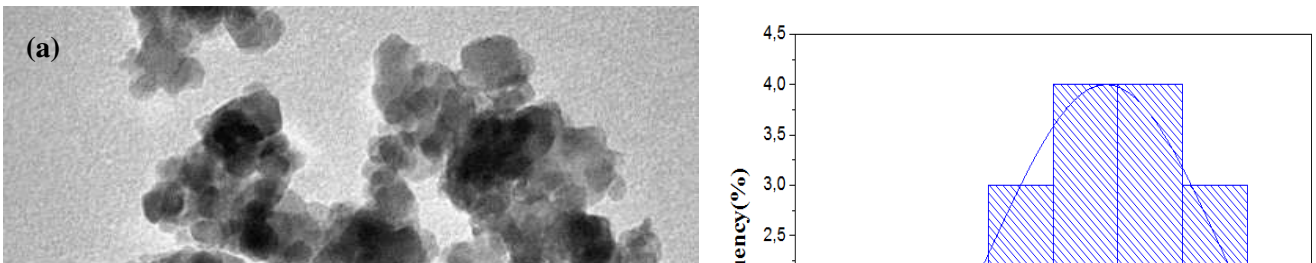

(b)

Fig 5. The TEM analysis and particles size distribution of the nanoparticle $ZnFe_{1.98}Gd_{0.01}Sm_{0.01}O_4$

In order further characterize the particle size and morphology of the sample, the TEM image of $ZnFe_{1.98}Gd_{0.01}Sm_{0.01}O_4$ nanoparticle was presented in Fig 5 (a) .The average particle sizes of sample were estimated by a statistical analysis using Image J software, which reveals that the particle size to be 16~24 nm, as shown in Fig. 5(b), The average particle size values are in good agreement with XRD pattern values. The TEM image confirms that the nanoparticle has spherical shape and agglomerated due to magnetic dipole interactions between the nanoparticle. These agglomerates can be able to increase the magnetic interaction, Fine particle size and high magnetism of Gd^{3+} and Sm^{3+} ions substituted zinc ferrite leads agglomeration of $ZnFe_{1.98}Gd_{0.01}Sm_{0.01}O_4$ nanoparticles .

4.5. Magnetic analysis

The Magnetic Property Measurement System (MPMS), was used to study the magnetic properties of sample, the **figure.6** shows the magnetic measurement of the hysteresis cycle at temperature 5k , 80k and 300k , under the external field applied $\mp$50 kOe. The **Figure.6** were used to obtain the saturation magnetization (Ms), the coercive field (Hc) and Mr/Ms magnetic moment (n_B) and anisotropy constant (K) . Their values are tabulated in **Table .4**. The values of the saturation magnetization Ms being deduced from the extrapolation of the curves $M\ vs.\ 1/H\ \ curves\ to\ \ 1/H\ \rightarrow 0$ [43].

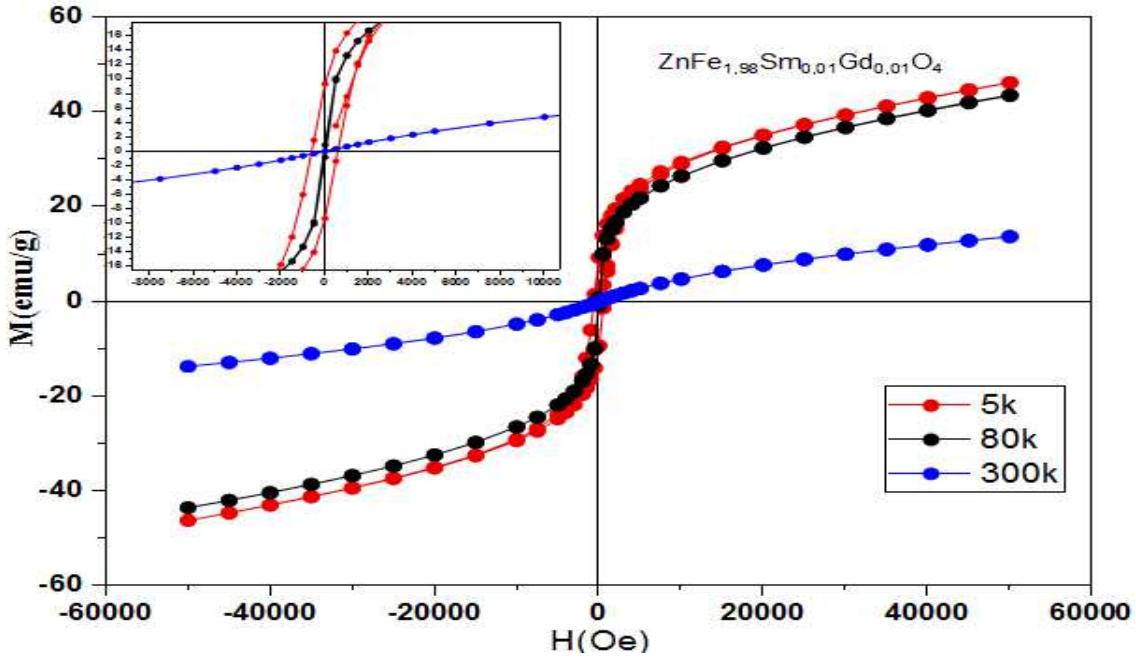

Fig.6. Hysteresis loops of sample $ZnFe_{1.98}Gd_{0.01}Sm_{0.01}O_4$

	$M_s(emu\ g^{-1})$	$M_r(emu\ g^{-1})$	$H_c(Oe)$	M_r/M_s	$n_B(Obs)$ (μ_B)
300K	18.9905	0	0	0	0.8263
80K	53.2743	0	0	0	2.318
5K	57.6932	9.3378	624.8896	0.1618	2.510

Table.4 All values obtained by magnetic measurements

The value of remanent magnetization and coercivity at room temperature and at 80 K are both zero, which proves that we are in the presence of superparamagnetic behavior. At 5 K a hysteresis cycle is observed, the M_s, M_r and H_c increase, in addition M_s and H_c become more pronounced, which proves a transition to a ferrimagnetic behavior, which originates from the cationic distribution, generated by the occupation of specific sites and the distribution between octahedral and tetrahedral sites and also from the particle size [44]. The increase of H_c at 5 K can be interpreted also by the non-compensation of exchange interactions between the three sub-lattices that make up the structure, and therefore the rotational magnetization

mechanism is present. The appearance of superparamagnetism at 80 K and 300 K indicates that magnetocrystalline anisotropy, which is important for maintaining magnetic ions in certain directions, is very low compared to the thermal energy. Zn^{2+} is diamagnetic in nature and have no unpaired electron. The only contribution to magneto-crystalline anisotropy comes from Fe^{3+}, Gd^{3+} and Sm^{3+} and may be insufficient to maintain the magnetic order in some directions. The presence of superparamagnetic also indicates that the thermal energy may have exceeded the blocking temperature, this part will be more clearly elucidated later.

Table 4. show that saturation magnetization decreased with temperature decreasing from 300K to 80k and 5 K. These three values are higher than those of undoped zinc ferrite. Whereas, according to the literature, for some undoped ferrites, a lower saturation magnetization was observed as shown in the **Table 5**. This can be explained that the magnetic property of spinel ferrite nanoparticles depends on several factors, such as cation substitution, the preparation process and crystallite size [45]. It should be noted that from the literature it has been reported that undoped $ZnFe_2O_4$ samples having a crystallite size between 4 and 12 nm show M_S values between 1.5 and 2.8 emu /g under the maximum applied magnetic field

	size	Ms (emu/g)	Hc(Oe)	ref
Co-precipitation	11	18.99	--	Present work
		10.35	--	[36]
	37	2.60	--	[25]
	11	20.34	9.314	[37]
Sol gel		1.47	317	[38]
		0.48	186	[39]
hydrothermal	32	34.37	--	[40]
		54.64	52	[41]
hydrolysis in a polyol medium	6	37.0	--	[42]
Ultrasound-assisted emulsion	12	25	--	[43]

(1T) [46].

Table. 5 The magnetic property values of $Zn\mathrm{Fe}_2\mathrm{O}_4$ prepared by different synthesis methods at 300 K.

In each case, that the spinel's zinc ferrite obtained from the same preparation technique and size

show on average comparable M_S values. From these works it is possible to confirm the influence of the synthesis method on chemical and physical properties of zinc ferrite. For example, the pure zinc ferrites obtained by sol-gel method have crystallite sizes between 13

and 38 nm, with M_S values between 0.72 to 3.4 emu/g, at an applied magnetic field 0.8 T [47], and that obtained by Ball milling method have crystallite sizes between 11 and 14 nm , with M_S values between 10 and 7.5 emu/g, at an applied magnetic field 0.7 T [48] . and that obtained by coprecipitation method have crystallite sizes between 11 and 37 nm with M_S values between 2.60 and 20.34 emu/g. The saturation magnetization varies closely with the particle size, the increase of which is manifested by a reduced displacement of the domain walls in the multi-domain range. This suggests that the increase in the Ms value with increasing particle size is significantly correlated with surface effects [49]. When temperature increases, The local structure of the particles, in term of cation distribution toward the tetrahedral and octahedral site of the spinel lattice. As a matter of fact, the partial migration of Fe^{3+} from sites B to A and conversely that of Zn^{2+} from sites A to B can lead to a decrease in magnetization in accordance with the ferrimagnetic Neel theory. It is also noted that magnetization decreases despite the presence of the paramagnetic ions Gd and Sm, this phenomenon can be explained by the fact that at high temperature, these ions attenuate the exchange interactions between Fe^{3+}-Fe^{3+} in the two sublattices. Gd^{3+} and Sm^{3+} ions are highly paramagnetic, thus by replacing Fe^{3+}, the super exchange strength decreases at the detriment of the paramagnetic ions. The magnetic behavior of spinel-type antiferromagnetic materials is largely governed by the negative Fe^{3+}-Fe^{3+} interaction (3d electron spin coupling). The RE^{3+}-Fe^{3+} interaction (4f-3d coupling) and the RE^{3+}- RE^{3+} one interaction (4f-5d-4f indirect electron spin coupling) exist, but are very weak [50]. In the literature it has been reported that 4f electrons from rare earths generally remain very localized in the solid and form the magnetic electrons [51]–[53] , all of which influence the bonding angles and distances.

in order to study the effect of exchange interactions in our sample a theoretical analysis was carried out. It is known that the magnetic interactions vary according to the bond angles and inversely proportional to the bond lengths, for these reasons, the distances and angles, cation-cation and cation-anion, were determined using the formulas presented in the **Table 9**.

Me − Me	Me − O	Bond angles
$\mathbf{b} = \frac{\sqrt{2}}{4}\mathbf{a}$	$p = a\left(\frac{5}{8} - u(\bar{4}3m)\right)$	$\theta_1 = \cos^{-1}\left(\frac{p^2 + q^2 - c^2}{2pq}\right)$
$\mathbf{c} = \frac{\sqrt{11}}{8}\mathbf{a}$	$q = a\sqrt{3}\left(u(\bar{4}3m) - \frac{1}{4}\right)$	$\theta_2 = \cos^{-1}\left(\frac{p^2 + r^2 - e^2}{2pr}\right)$
$\mathbf{d} = \frac{\sqrt{3}}{4}\mathbf{a}$	$r = a\sqrt{11}\left(u(\bar{4}3m) - \frac{1}{4}\right)$	$\theta_3 = \cos^{-1}\left(\frac{2p^2 - b^2}{2p^2}\right)$
$\mathbf{e} = \frac{3\sqrt{3}}{8}\mathbf{a}$	$s = a\sqrt{3}\left(\frac{u(\bar{4}3m)}{3} + \frac{1}{8}\right)$	$\theta_4 = \cos^{-1}\left(\frac{p^2 + s^2 - f^2}{2ps}\right)$
$\mathbf{f} = \frac{\sqrt{6}}{4}\mathbf{a}$		$\theta_5 = \cos^{-1}\left(\frac{r^2 + q^2 - d^2}{2rq}\right)$

Table 9. Expressions for determining the cation–cation and cation–anion distances, and the bond angles

From **Table 10** it is observed that the bond lengths between Me-O (r, q and s) and Me-Me (b to f) increased, while q decreases by doping with Sm^{3+} and Gd^{3+}. An increase in the site radius can be predicted due to the substitution of the small Fe $^{3+}$ (0.067 nm) ions by larger Sm^{3+} (0.096 nm) and Gd^{3+}(0.094 nm) ions in the octahedral sites. The ionic radius of a Gd^{3+} and Sm^{3+}, which is large for the tetrahedral site and therefore Gd^{3+} and Sm^{3+} ions are compelled to occupy octahedral sites.

The calculated values of bond angles have been listed in **Table 11**. It has been found that θ_1, θ_2 and θ_5 decrease while θ_3 and θ_4 increase compared with the result found in the literature [54]. The decrease in bond angles (θ_1, θ_2 and θ_5) indicate a decrease in the strength of A-B, A-A exchange interactions and the increase in bond angles (θ_3, θ_4) indicates increase in the strength of B-B exchange interactions. Theoretical investigation of bond angles indicates the dominance of A-B super-exchange and B-B exchange interaction for sample. This is due to the insertion of Gd^{3+} and Sm^{3+} ions at octahedral sites, which increases the strength of B-B exchange interaction. From this it can be deduced that the Fe^{3+}, Sm^{3+} and Gd^{3+} ions on the B sites, reinforce the B-B super-exchange interactions, which leads to the improvement of magnetic properties. This enhancement in the magnetic properties is also attributed to the higher magnetic moment of Gd^{3+} (7 μ_B) and Sm^{3+} (0.71 μ_B) who are having a high spin magnetic moment compared to that of Fe^{3+} (5μ_B) [55], [56].

to understand the correlation of magnetic properties with the characteristics of nanoparticles. The variation of magnetization as a function of temperature provided us with this information. The blocking temperature T_B, which reflects the transition from the superparamagnetic state to the blocked state, is determined from the position of the MZFC peak, whose widening

provides information on the degree of particle size distribution, since blocking temperatures are closely associated with the variation of nanoparticle sizes [57] . It should be noted that information on the structural disorder of nanoparticles can also be obtained from the temperature corresponding to the convergence of the MZFC and MFC curves. i.e. the irreversible temperature (T_{irr}), and its distance from T_B [32] .

Parameters	b(Å)	c(Å)	d(Å)	e(Å)	f(Å)	p(Å)	q(Å)	r(Å)	s(Å)	ref
$ZnFe_{1.98}Sm_{0.01G}d_{0.01}O_4$	2.9819	3.4965	3.6420	5.4781	5.1648	2.0258	1.6991	3.7707	3.6997	Present work
$ZnFe_2O_4$	2.9663	3.4783	3.6329	5.4494	5.1378	2.0096	1.9687	3.7697	6.6837	[54]

Table 10.The calculated inter-ionic distances between cation–anion (Me–O) and cation–

Parameters	$\theta_1(°)$	$\theta_2(°)$	$\theta_3(°)$	$\theta_4(°)$	$\theta_5(°)$	ref
$ZnFe_{1.98}(SmGd)_{0.01}O_4$	122.1374	139.9039	94.7761	126.3380	71.3114	Present work
$ZnFe_2O_4$	122.25	140.38	94.57	126.29	71.62	[54]

cation (Me–Me) of sample $ZnFe_{1.98}Gd_{0.01}Sm_{0.01}O_4$

Table.11 The calculated bond angle of sample $ZnFe_{1.98}Gd_{0.01}Sm_{0.01}O_4$

Fig. 7 shows zero field cooled magnetization (MZFC) and field cooled magnetization (MFC) curves of $ZnFe_{1.98}(GdSm)_{0.01}O_4$, measured in the temperature range of 4-300 K under an applied field of 100 Oe. When the temperature increases in the MZFC measurement, an increase in magnetization has been observed up to a maximum value at a specific critical temperature T_B = 55 K, called the blocking temperature (T_B). Above T_B in the unblocked region, the MZFC monotonically decreases with increasing temperature. This is the characteristic behavior of superparamagnetic materials[58]. These results are in perfect agreement with the M-H hysteresis loops measurements, in fact the hysteresis loops measured at 80 and 300 K, temperatures greater than the Block temperature 55 K, do not exhibit hysteresis, which proves that we are in the presence of superparamagnetic behavior, while at 5 K the behavior is ferrimagnetic.

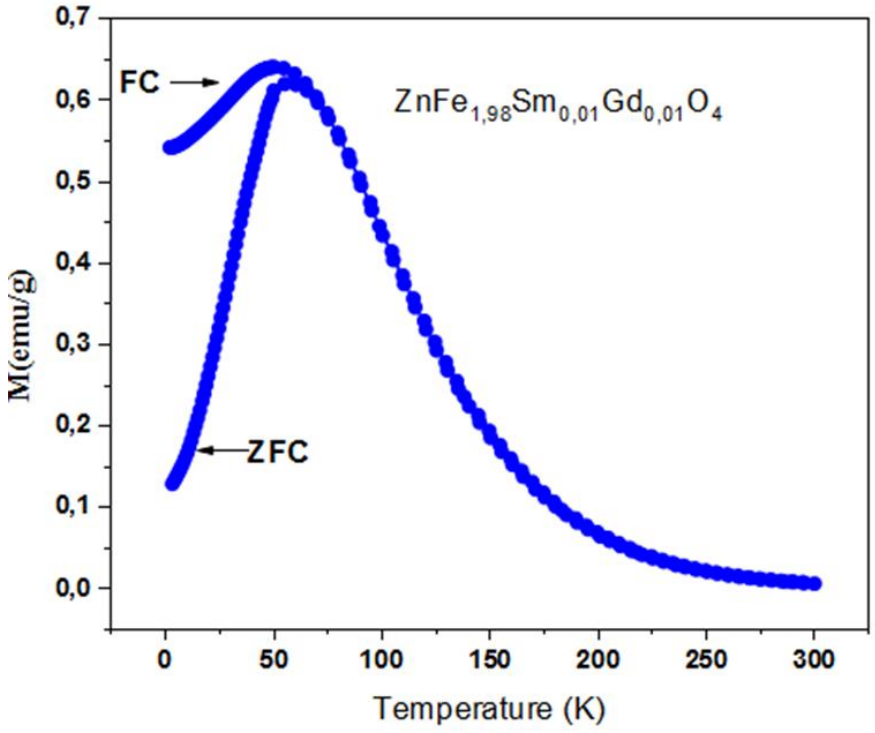

Figure.8 Zero field cooled and field cooled magnetization vs. temperature recorded in an external field of 100 Oe

The MZFC and MFC measurements of the sample show an irreversible magnetic behavior below the temperature, the so-called irreversibility temperature T_{irr}. T_{irr} is defined as the temperature of the divergence between the MZFC and MFC curves, and corresponds to the blocking temperature of the largest nanoparticles in superparamagnetic materials[59] [60]. The work of Klemens Rumpf et al [61] has been very significant, showing that the decrease in the concentration of the particle solution results in a weakening of the magnetic coupling between the particles, which leads to a shift of the blocking temperature towards lower values, and that the decrease in particle size also leads to a decrease of the blocking temperature.

The most specific results in this work is the obtaining of Gd^{3+} and Sm^{3+} co-doped zinc nanoferrites, having a blocking temperature much higher than that of pure zinc ferrite, a result which is rarely obtained in other works. It should be noted that blocking temperature of undoped zinc ferrite by a novel multi-step homogeneous non-aqueous solution synthesis method is T_B= 6 K [62]. Indeed, little work has been dedicated to the effect of rare earth doping on the blocking temperature, such as that of M. Bini et al for $ZnFe_{1.9}Gd_{0.1}O_4$ synthesized by microwave combustion method [32] who reported that T_B= 32 K, . The improve in T_B of the sample can be explained by the larger degree of cation inversion of the sample synthesized at lower temperatures, resulting by larger magnetic anisotropy [63]. On

the other hand, the high magnetic moments and high magnetocrystalline anisotropy at low temperature that characterize Rare Earth (RE) elements due to the localized nature of the 4f electrons. Indeed, doping with small amounts of rare earth (RE) elements can improve the magnetic properties, especially the T_B of nanoferrites. Although a Gd^{3+} ion has a zero orbital angular momentum, it has been reported in the literature that Gd contributes to and enhances the anisotropy [64].

The experimental values of magnetic moment per formula unit n_B of $ZnFe_{1.98}Gd_{0.01}Sm_{0.01}O_4$was be calculated by using following relation [59] :

$$n_B = \frac{M \times M_s}{5585} (9)$$

Where M is the molecular weight of the sample, Ms is the saturation magnetization. The values of magnetic moments are 0.8263 μ_B at 300 K, 2.318 at 80 K and 2.510 μ_B at 5 K. The magnetic moment n_B is proportional to the saturation magnetization (M_s), so with the decrease in Ms, the value of the magnetic moment $n_B$also decreases.

The variation of magnetic moment n_B can be explained with Néel's theory. The magnetic moment of Fe^{3+}, Zn^{2+}, Sm^{3+} and Gd^{3+} ions are 5 μ_B, 0 μ_B, 0.71 μ_B and 7 μ_B, respectively. According to two sublattice models of Neel's theory[65], and using the cation distribution:

$$[\boldsymbol{Zn_{0.57}Fe_{0.43}}]^{\boldsymbol{A}}\ [\boldsymbol{Zn_{0.43}Fe_{1.55}(SmGd)_{0.01}}]^{\boldsymbol{B}}$$

Therefore, the theoretic magnetic moment per formula unit in μ_B, $n_B(cal)$, is described as :

$$\boldsymbol{n_B(cal) = M_B - M_A = 5.6 + \sum X_i \mu_{REi} = 5.6 + 0.01\mu_{Sm^{3+}} + 0.01\mu_{Gd^{3+}}}\ \textbf{(10)}$$

The net magnetic moment, $n_B(cal)$ has been calculated using the equation $n_B(cal)$ = M_B- M_A where M_A and M_B are magnetizations of A and B sublattices, $\boldsymbol{X_i}$ is the stoichiometric concentration of the rare earth element RE_i for us RE_1=Gd^{3+}, RE_2=Sm^{3+}, μRE_i is the magnetic moment of rare earth element. As shown from the formula, the magnetization varies with the doping concentration and the relative moments of the rare earth elements, their growth causes the magnetization to grow. the calculated values $n_B(cal)$ is 5.6771 μ_B at T= 0 K, we note that this value, calculated at T= 0 K, is comparable to that determined experimentally $n_B(Obs)$ = 2.510 μ_B at 5K (**table. 5**), therefore the theoretical value corroborates well the experimental value which justifies the cationic distribution determined.

The squareness ratios R = Mr/Ms were calculated for the $ZnFe_{1.98}Gd_{0.01}Sm_{0.01}O_4$ nanoparticles at 5 K is 0.1618 suggesting that the particles are predominantly not in the

single-domain state, even in the case of nanoparticles. Stoner and Wohlfarth [61] have reported the ratio R=Mr/Ms=0.5 for non-interacting randomly oriented particles that are undergoing coherent rotation, while for R<0.5 the particles interact via magnetostatic interactions. In addition, R is less than 0.50, the phenomenon can be attributed to surface spin disorder effects. The particles are smaller and then exhibit a greater surface contribution.

5. Conclusion

Gd^{3+}, Sm^{3+} co-doped Zinc ferrite nanoparticles with a single-phase cubic spinel structure were successfully prepared by coprecipitation method. Rietveld refinement of the XRD patterns indicated that the lattice parameter is in relatively good agreement with those found in the literature. confirming the accommodation of the larger Gd^{3+} and Sm^{3+} ions in the Zinc ferrite spinel. The calculated crystallite size from XRD indicates a decrease compared to non-opted zinc ferrite. The estimated cation distribution shows that Gd^{3+} and Sm^{3+} ions have strong preferences towards octahedral B-sites, whereas Zn^{2+} and Fe^{3+} ions are distributed over the available sites. The absorption bands in FTIR spectra confirmed the formation of the structure spinel. The prepared nanoparticles have spherical morphology and are slightly agglomerated as confirmed by TEM analysis. MPMS results show the superparamagnetic nature at 80 and 300 K, and weak ferrimagnetic behavior at 5 K. Saturation magnetization studied at 5 K, 80 K and at 300 K shows a decrease from 57.6932 to 18.9905 ($\mathrm{emu.\,g^{-1}}$) with the Gd^{3+}, Sm^{3+} co-doping in the Zinc ferrite. The ZFC and FC curves show a peak corresponding to the blocking temperature at T_B= 55 K. Consequently, this work has demonstrated a close relationship between the observed magnetic properties of $ZnFe_{1.98}Gd_{0.01}Sm_{0.01}O_4$nanoparticles and their morphology and local structure.

Conflicts of interest

There are no conflicts to declare.

Acknowledgements

This research did not receive any specific grant from funding agencies in the public, commercial, or not-for-profit sectors.

Reference:

[1] S. Bae *et al.*, « Miniaturized broadband ferrite T-DMB antenna for mobile-phone applications », *IEEE Trans. Magn.*, vol. 46, n° 6, p. 2361–2364, 2010.

[2] F. Farzami, K. Forooraghi, et M. Norooziarab, « Miniaturization of a microstrip antenna using a compact and thin magneto-dielectric substrate », *IEEE Antennas Wirel. Propag. Lett.*, vol. 10, p. 1540–1542, 2011.

[3] J. Lee *et al.*, « Broadband bluetooth antenna based on Co2Z hexaferrite-glass composite », *Microw. Opt. Technol. Lett.*, vol. 53, n° 6, p. 1222–1225, 2011.
[4] P. M. Ikonen, K. N. Rozanov, A. V. Osipov, P. Alitalo, et S. A. Tretyakov, « Magnetodielectric substrates in antenna miniaturization: Potential and limitations », *IEEE Trans. Antennas Propag.*, vol. 54, n° 11, p. 3391–3399, 2006.
[5] J. Wang *et al.*, « Self Biased Y-Junction Circulator at $${$$\backslash$rm K$}$ _ ${$$\backslash$rm u$}$ $ Band », *IEEE Microw. Wirel. Compon. Lett.*, vol. 21, n° 6, p. 292–294, 2011.
[6] B. K. O'Neil et J. L. Young, « Experimental investigation of a self-biased microstrip circulator », *IEEE Trans. Microw. Theory Tech.*, vol. 57, n° 7, p. 1669–1674, 2009.
[7] S. D. Yoon, J. Wang, N. Sun, C. Vittoria, et V. G. Harris, « Ferrite-coupled line circulator simulations for application at X-band frequency », *IEEE Trans. Magn.*, vol. 43, n° 6, p. 2639–2641, 2007.
[8] C. K. Seewald et J. R. Bray, « Ferrite-filled antisymmetrically biased rectangular waveguide isolator using magnetostatic surface wave modes », *IEEE Trans. Microw. Theory Tech.*, vol. 58, n° 6, p. 1493–1501, 2010.
[9] J. Wu, M. Li, X. Yang, S. Beguhn, et N. X. Sun, « A Novel Tunable Planar Isolator with Serrated Microstrip Structure », *IEEE Trans. Magn.*, vol. 48, n° 11, p. 4371–4374, 2012.
[10] S. Capraro *et al.*, « Feasibility of an integrated self biased coplanar isolator with barium ferrite films », *IEEE Trans. Compon. Packag. Technol.*, vol. 30, n° 3, p. 411–415, 2007.
[11] J.-J. Lee *et al.*, « High-Quality Factor Ni-Zn Ferrite Planar Inductor », *IEEE Trans. Magn.*, vol. 46, n° 6, p. 2417-2420, juin 2010, doi: 10.1109/TMAG.2010.2044377.
[12] C. Yang *et al.*, « Investigation of on-chip soft-ferrite-integrated inductors for RF ICs—Part I: Design and simulation », *IEEE Trans. Electron Devices*, vol. 56, n° 12, p. 3133–3140, 2009.
[13] K. Naishadham, « Closed-form design formulas for the equivalent circuit characterization of ferrite inductors », *IEEE Trans. Electromagn. Compat.*, vol. 53, n° 4, p. 923–932, 2011.
[14] I. Kowase, T. Sato, K. Yamasawa, et Y. Miura, « A planar inductor using Mn-Zn ferrite/polyimide composite thick film for low-Voltage and large-current DC-DC converter », *IEEE Trans. Magn.*, vol. 41, n° 10, p. 3991–3993, 2005.
[15] V. Loyau, G.-Y. Wang, M. L. Bue, et F. Mazaleyrat, « An analysis of Mn-Zn ferrite microstructure by impedance spectroscopy, scanning transmission electron microscopy and energy dispersion spectrometry characterizations », *J. Appl. Phys.*, vol. 111, n° 5, p. 053928, 2012.
[16] R. P. Patil, S. D. Delekar, D. R. Mane, et P. P. Hankare, « Synthesis, structural and magnetic properties of different metal ion substituted nanocrystalline zinc ferrite », *Results Phys.*, vol. 3, p. 129–133, 2013.
[17] H. J. Glass et G. de With, « Fractal characterization of the compaction and sintering of ferrites », *Mater. Charact.*, vol. 47, n° 1, p. 27–37, 2001.
[18] G. Kogias, V. Tsakaloudi, P. Van der Valk, et V. Zaspalis, « Improvement of the properties of MnZn ferrite power cores through improvements on the microstructure of the compacts », *J. Magn. Magn. Mater.*, vol. 324, n° 2, p. 235–241, 2012.
[19] J. C. Maurya, P. S. Janrao, A. A. Datar, N. S. Kanhe, S. V. Bhoraskar, et V. L. Mathe, « Evidence of domain wall pinning in aluminum substituted cobalt ferrites », *J. Magn. Magn. Mater.*, vol. 412, p. 164–171, 2016.
[20] M. Hashim, S. Kumar, S. E. Shirsath, R. K. Kotnala, J. Shah, et R. Kumar, « Synthesis and characterizations of Ni2+ substituted cobalt ferrite nanoparticles », *Mater. Chem. Phys.*, vol. 139, n° 2-3, p. 364–374, 2013.
[21] A. Rahman, Y. Ng M, A. U. Ahmed, T. Alam, M. J. Singh, et M. T. Islam, « A compact 5G antenna printed on manganese zinc ferrite substrate material », *IEICE Electron. Express*, vol. 13, n° 11, p. 20160377–20160377, 2016.
[22] V. Naidu, R. A. Rahim, J. Dhinakaran, G. V. Devi, et H. R. Suresh, « Sm-Gd doped Magnesium Ferrite for E-shaped Microstrip Patch Antenna », *Int. J. Comput. Appl.*, vol. 35, n° 4, 2011.
[23] K. V. Koleva, N. I. Velinov, T. S. Tsoncheva, I. G. Mitov, et B. N. Kunev, « Preparation, structure and catalytic properties of ZnFe2O4 », p. 6.

[24] M. M. L. Sonia, S. Anand, V. M. Vinosel, M. A. Janifer, S. Pauline, et A. Manikandan, « Effect of lattice strain on structure, morphology and magneto-dielectric properties of spinel NiGdxFe2−xO4 ferrite nano-crystallites synthesized by sol-gel route », *J. Magn. Magn. Mater.*, vol. 466, p. 238-251, nov. 2018, doi: 10.1016/j.jmmm.2018.07.017.
[25] T. R. Tatarchuk *et al.*, « Effect of cobalt substitution on structural, elastic, magnetic and optical properties of zinc ferrite nanoparticles », *J. Alloys Compd.*, vol. 731, p. 1256-1266, janv. 2018, doi: 10.1016/j.jallcom.2017.10.103.
[26] D. M. Ghone, V. L. Mathe, K. K. Patankar, et S. D. Kaushik, « Microstructure, lattice strain, magnetic and magnetostriction properties of holmium substituted cobalt ferrites obtained by co-precipitation method », *J. Alloys Compd.*, vol. 739, p. 52-61, mars 2018, doi: 10.1016/j.jallcom.2017.12.219.
[27] X. Zhao, W. Wang, Y. Zhang, S. Wu, F. Li, et J. P. Liu, « Synthesis and characterization of gadolinium doped cobalt ferrite nanoparticles with enhanced adsorption capability for Congo Red », *Chem. Eng. J.*, vol. 250, p. 164-174, août 2014, doi: 10.1016/j.cej.2014.03.113.
[28] J. Singh, S. Sharma, S. Sharma, et R. C. Singh, « Effect of tungsten doping on structural and optical properties of rutile TiO2 and band gap narrowing », *Optik*, vol. 182, p. 538-547, avr. 2019, doi: 10.1016/j.ijleo.2019.01.070.
[29] S. M. Masoudpanah, S. A. Seyyed Ebrahimi, M. Derakhshani, et S. M. Mirkazemi, « Structure and magnetic properties of La substituted ZnFe2O4 nanoparticles synthesized by sol–gel autocombustion method », *J. Magn. Magn. Mater.*, vol. 370, p. 122-126, déc. 2014, doi: 10.1016/j.jmmm.2014.06.062.
[30] R. S. Yadav *et al.*, « Influence of Gd3+-substitution on structural, magnetic, dielectric and modulus spectroscopic characteristics of ZnFe2O4 spinel ferrite nanoparticles », *J. Mater. Sci. Mater. Electron.*, vol. 29, n° 18, p. 15878-15893, sept. 2018, doi: 10.1007/s10854-018-9674-z.
[31] A. N. Birgani, M. Niyaifar, et A. Hasanpour, « Study of cation distribution of spinel zinc nano-ferrite by X-ray », *J. Magn. Magn. Mater.*, vol. 374, p. 179–181, 2015.
[32] M. Bini, C. Tondo, D. Capsoni, M. C. Mozzati, B. Albini, et P. Galinetto, « Superparamagnetic ZnFe 2 O 4 nanoparticles: The effect of Ca and Gd doping », *Mater. Chem. Phys.*, vol. 204, p. 72-82, janv. 2018, doi: 10.1016/j.matchemphys.2017.10.033.
[33] R. Islam, M. A. Hakim, M. O. Rahman, H. Narayan Das, et M. A. Mamun, « Study of the structural, magnetic and electrical properties of Gd-substituted Mn–Zn mixed ferrites », *J. Alloys Compd.*, vol. 559, p. 174-180, mai 2013, doi: 10.1016/j.jallcom.2012.12.080.
[34] V. Jagadeesha Angadi, B. Rudraswamy, K. Sadhana, et K. Praveena, « Effect of Sm3+-Gd3+ co-doping on dielectric properties of Mn-Zn ferrites synthesized via combustion route », *Mater. Today Proc.*, vol. 3, n° 6, p. 2178-2186, 2016, doi: 10.1016/j.matpr.2016.04.124.
[35] A. Kumar, P. S. Rana, M. S. Yadav, et R. P. Pant, « Effect of Gd3+ ion distribution on structural and magnetic properties in nano-sized Mn–Zn ferrite particles », *Ceram. Int.*, vol. 41, n° 1, p. 1297-1302, janv. 2015, doi: 10.1016/j.ceramint.2014.09.060.
[36] Y. Y. Meng *et al.*, « Structure and magnetic properties of Mn(Zn)Fe2−xRExO4 ferrite nano-powders synthesized by co-precipitation and refluxing method », *Powder Technol.*, vol. 229, p. 270-275, oct. 2012, doi: 10.1016/j.powtec.2012.06.050.
[37] K. Kamazawa, Y. Tsunoda, K. Odaka, et K. Kohn, « Spin liquid state in ZnFe2O4 », *J. Phys. Chem. Solids*, vol. 60, n° 8-9, p. 1261-1264, sept. 1999, doi: 10.1016/S0022-3697(99)00099-2.
[38] M. Atif, S. K. Hasanain, et M. Nadeem, « Magnetization of sol–gel prepared zinc ferrite nanoparticles: Effects of inversion and particle size », *Solid State Commun.*, vol. 138, n° 8, p. 416-421, mai 2006, doi: 10.1016/j.ssc.2006.03.023.
[39] C. B. Kolekar, P. N. Kamble, et A. S. Vaingankar, « Structural and dc electrical resistivity study of Gd3+-substituted Cu-Cd mixed ferrites », *J. Magn. Magn. Mater.*, vol. 138, n° 1, p. 211-215, nov. 1994, doi: 10.1016/0304-8853(94)90418-9.
[40] M. Satalkar et S. N. Kane, « On the study of Structural properties and Cation distribution of $Zn_{0.75-x}Ni_xMg_{0.15}Cu_{0.1}Fe_2O_4$ nano ferrite: Effect of Ni addition », *J. Phys. Conf. Ser.*, vol. 755, p. 012050, oct. 2016, doi: 10.1088/1742-6596/755/1/012050.

[41] S. Torkian, A. Ghasemi, et R. S. Razavi, « Structural and Magnetic Consequences of Mn0.6Zn0.4Fe2−x Gd x O4 Ferrite », *J. Supercond. Nov. Magn.*, vol. 29, n° 6, p. 1617-1625, juin 2016, doi: 10.1007/s10948-016-3458-6.
[42] K. Yang, H. Peng, Y. Wen, et N. Li, « Re-examination of characteristic FTIR spectrum of secondary layer in bilayer oleic acid-coated Fe3O4 nanoparticles », *Appl. Surf. Sci.*, vol. 256, n° 10, p. 3093-3097, mars 2010, doi: 10.1016/j.apsusc.2009.11.079.
[43] El. Abouzir, M. Elansary, M. Belaiche, et H. Jaziri, « Magnetic and structural properties of single-phase Gd $^{3+}$ -substituted Co–Mg ferrite nanoparticles », *RSC Adv.*, vol. 10, n° 19, p. 11244-11256, 2020, doi: 10.1039/D0RA01841D.
[44] Y. Mouhib, M. Belaiche, et S. Briche, « Elaboration, Characterization, and Magnetic Properties of Ni $_{0.5}$ Zn $_{0.5}$ Fe $_{2}$ O $_{4}$ Nanoparticles of High Purity Using Molten Salts Technique », *Phys. Status Solidi A*, vol. 215, n° 23, p. 1800469, déc. 2018, doi: 10.1002/pssa.201800469.
[45] R. S. Yadav *et al.*, « Sonochemical synthesis of Gd3+ doped CoFe2O4 spinel ferrite nanoparticles and its physical properties », *Ultrason. Sonochem.*, vol. 40, p. 773-783, janv. 2018, doi: 10.1016/j.ultsonch.2017.08.024.
[46] M. K. Lima-Tenório, E. T. Tenório-Neto, A. A. W. Hechenleitner, H. Fessi, et E. A. G. Pineda, « CoFe₂O₄ and ZnFe₂O₄ Nanoparticles: An Overview About Structure, Properties, Synthesis and Biomedical Applications », *J. Colloid Sci. Biotechnol.*, vol. 5, n° 1, p. 45-54, mars 2016, doi: 10.1166/jcsb.2016.1135.
[47] M. Gharagozlou et R. Bayati, « Low temperature processing and magnetic properties of zinc ferrite nanoparticles », *Superlattices Microstruct.*, vol. 78, p. 190-200, févr. 2015, doi: 10.1016/j.spmi.2014.12.004.
[48] C. N. Chinnasamy, A. Narayanasamy, N. Ponpandian, K. Chattopadhyay, H. Guérault, et J.-M. Greneche, « Magnetic properties of nanostructured ferrimagnetic zinc ferrite », *J. Phys. Condens. Matter*, vol. 12, n° 35, p. 7795–7805, août 2000, doi: 10.1088/0953-8984/12/35/314.
[49] I. Sharifi, H. Shokrollahi, M. M. Doroodmand, et R. Safi, « Magnetic and structural studies on CoFe2O4 nanoparticles synthesized by co-precipitation, normal micelles and reverse micelles methods », *J. Magn. Magn. Mater.*, vol. 324, n° 10, p. 1854-1861, mai 2012, doi: 10.1016/j.jmmm.2012.01.015.
[50] N. Rezlescu, E. Rezlescu, C. Pasnicu, et M. L. Craus, « Effects of the rare-earth ions on some properties of a nickel-zinc ferrite », *J. Phys. Condens. Matter*, vol. 6, n° 29, p. 5707–5716, juill. 1994, doi: 10.1088/0953-8984/6/29/013.
[51] D. W. Boys et S. Legvold, « Thermal Conductivities and Lorenz Functions of Dy, Er, and Lu Single Crystals », *Phys. Rev.*, vol. 174, n° 2, p. 377-384, oct. 1968, doi: 10.1103/PhysRev.174.377.
[52] W. J. Nellis et S. Legvold, « Thermal Conductivities and Lorenz Functions of Gadolinium, Terbium, and Holmium Single Crystals », *Phys. Rev.*, vol. 180, n° 2, p. 581-590, avr. 1969, doi: 10.1103/PhysRev.180.581.
[53] B. Zhou, Y.-W. Zhang, C.-S. Liao, C.-H. Yan, L.-Y. Chen, et S.-Y. Wang, « Rare-earth-mediated magnetism and magneto-optical Kerr effects in nanocrystalline CoFeMn0.9RE0.1O4 thin films », *J. Magn. Magn. Mater.*, vol. 280, n° 2, p. 327-333, sept. 2004, doi: 10.1016/j.jmmm.2004.03.031.
[54] A. I. Borhan, A. R. Iordan, et M. N. Palamaru, « Correlation between structural, magnetic and electrical properties of nanocrystalline Al3+ substituted zinc ferrite », *Mater. Res. Bull.*, vol. 48, n° 7, p. 2549-2556, juill. 2013, doi: 10.1016/j.materresbull.2013.03.012.
[55] X. Wu, Z. Ding, N. Song, L. Li, et W. Wang, « Effect of the rare-earth substitution on the structural, magnetic and adsorption properties in cobalt ferrite nanoparticles », *Ceram. Int.*, vol. 42, n° 3, p. 4246-4255, févr. 2016, doi: 10.1016/j.ceramint.2015.11.100.
[56] T. Sodaee, A. Ghasemi, et R. Shoja Razavi, « Cation distribution and microwave absorptive behavior of gadolinium substituted cobalt ferrite ceramics », *J. Alloys Compd.*, vol. 706, p. 133-146, juin 2017, doi: 10.1016/j.jallcom.2017.02.233.
[57] E. C. Mendonça, C. B. R. Jesus, W. S. D. Folly, C. T. Meneses, et J. G. S. Duque, « Size Effects on the Magnetic Properties of ZnFe2O4 Nanoparticles », *J. Supercond. Nov. Magn.*, vol. 26, n° 6, p. 2329-2331, juin 2013, doi: 10.1007/s10948-012-1426-3.

[58] R. K. Zheng, H. Gu, B. Xu, et X. X. Zhang, « The origin of the non-monotonic field dependence of the blocking temperature in magnetic nanoparticles », *J. Phys. Condens. Matter*, vol. 18, n° 26, p. 5905–5910, juin 2006, doi: 10.1088/0953-8984/18/26/010.
[59] A. Franco et F. C. e Silva, « High temperature magnetic properties of cobalt ferrite nanoparticles », *Appl. Phys. Lett.*, vol. 96, n° 17, p. 172505, avr. 2010, doi: 10.1063/1.3422478.
[60] L. Maldonado-Camargo, M. Unni, et C. Rinaldi, « Magnetic Characterization of Iron Oxide Nanoparticles for Biomedical Applications », *Methods Mol. Biol. Clifton NJ*, vol. 1570, p. 47-71, 2017, doi: 10.1007/978-1-4939-6840-4_4.
[61] K. Rumpf, P. Granitzer, P. M. Morales, P. Poelt, et M. Reissner, « Variable blocking temperature of a porous silicon/Fe3O4 composite due to different interactions of the magnetic nanoparticles », *Nanoscale Res. Lett.*, vol. 7, n° 1, p. 445, août 2012, doi: 10.1186/1556-276X-7-445.
[62] L. D. Tung *et al.*, « Annealing effects on the magnetic properties of nanocrystalline zinc ferrite », *Phys. B Condens. Matter*, vol. 319, n° 1, p. 116-121, juill. 2002, doi: 10.1016/S0921-4526(02)01114-6.
[63] X. Guo *et al.*, « $ZnFe_2O_4$ Nanotubes: Microstructure and Magnetic Properties », *J. Phys. Chem. C*, vol. 118, n° 51, p. 30145-30152, déc. 2014, doi: 10.1021/jp507991e.
[64] B. A. Calhoun et M. J. Freiser, « Anisotropy of gadolinium iron garnet », *J. Appl. Phys.*, vol. 34, n° 4, p. 1140–1145, 1963.
[65] G. D. Tang *et al.*, « Three models of magnetic ordering in typical magnetic materials », *Phys. Rep.*, vol. 758, p. 1-56, oct. 2018, doi: 10.1016/j.physrep.2018.06.009.

Figures

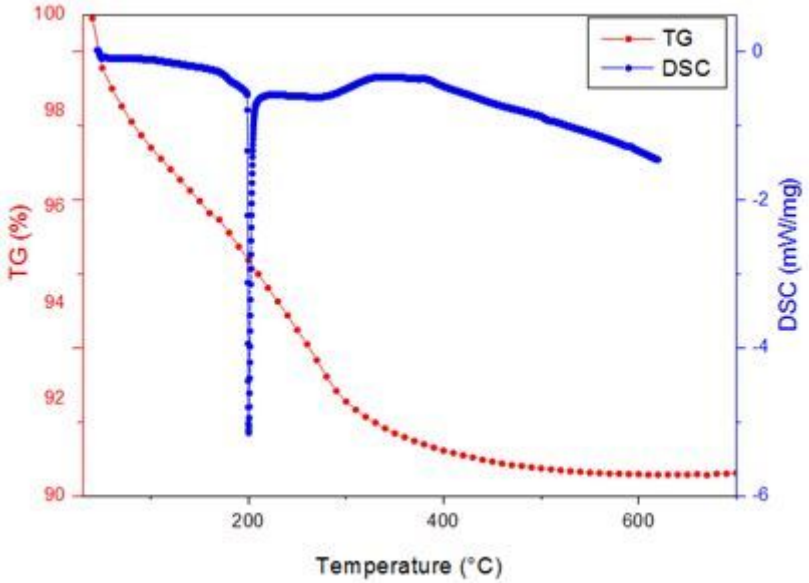

Figure 1

Thermal analysis of the polymeric and nitrate precursors

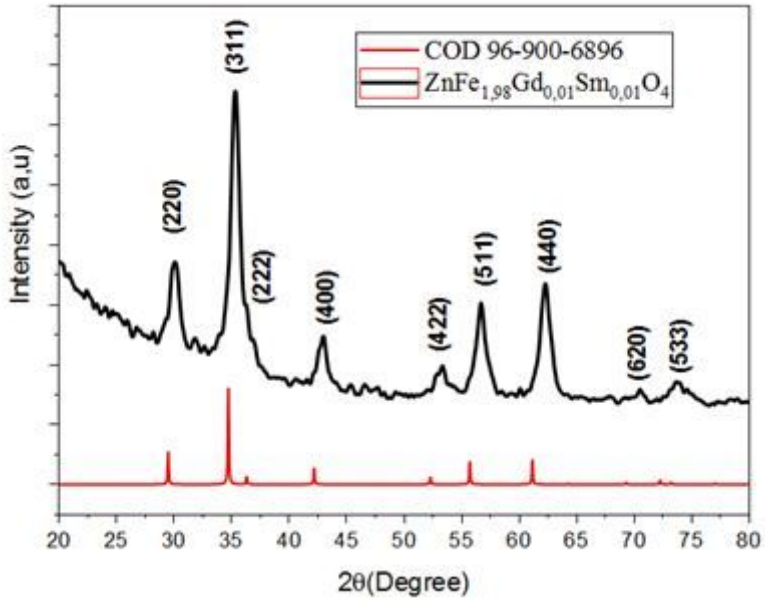

Figure 2

Patterns (XRD) ofZnFe_1.98 □□Gd□_0.01 Sm□_0.01 O_4calcined at 700° C

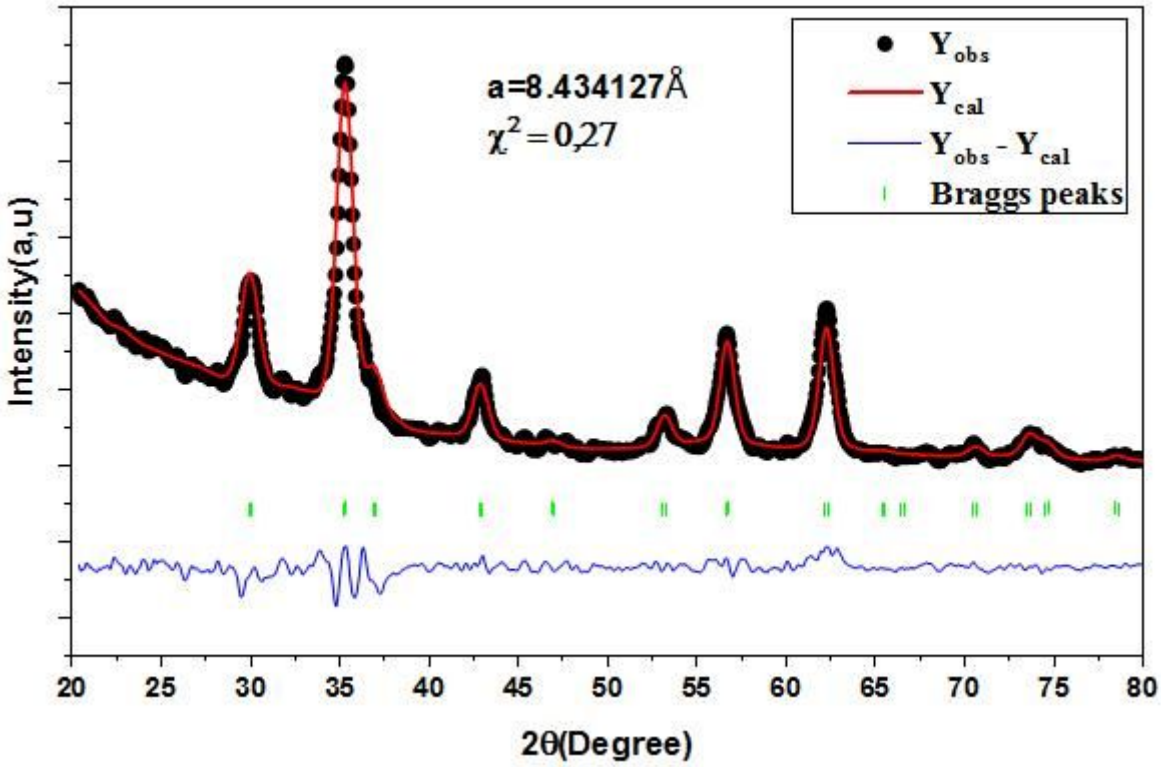

Figure 3

Rietveld refined XRD pattern for the ZnFe_1.98 □□Gd□_0.01 Sm□_0.01 O_4 sample

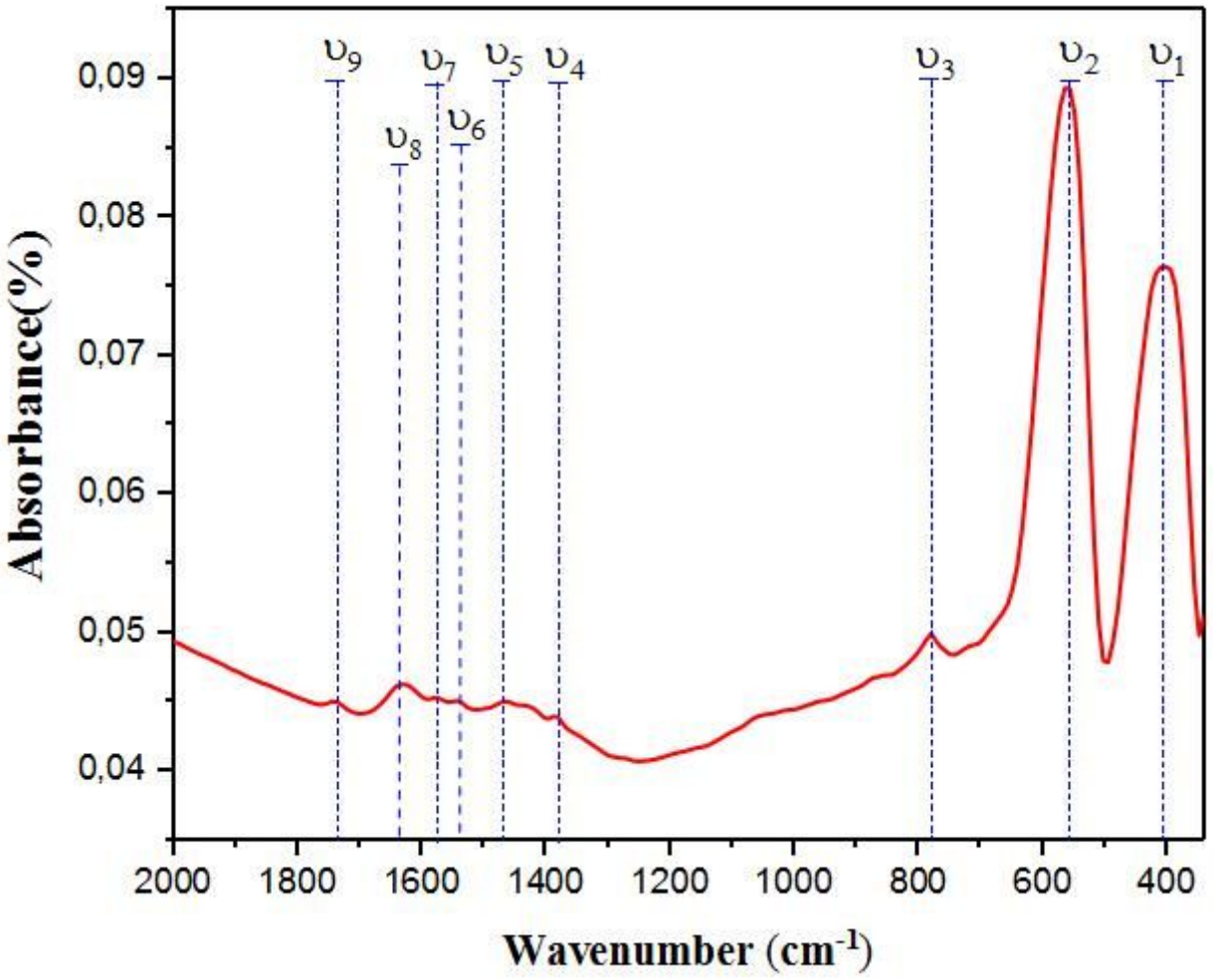

Figure 4

FTIR spectra of sample ZnFe_1.98 □□Gd□_0.01 Sm□_0.01 O_4

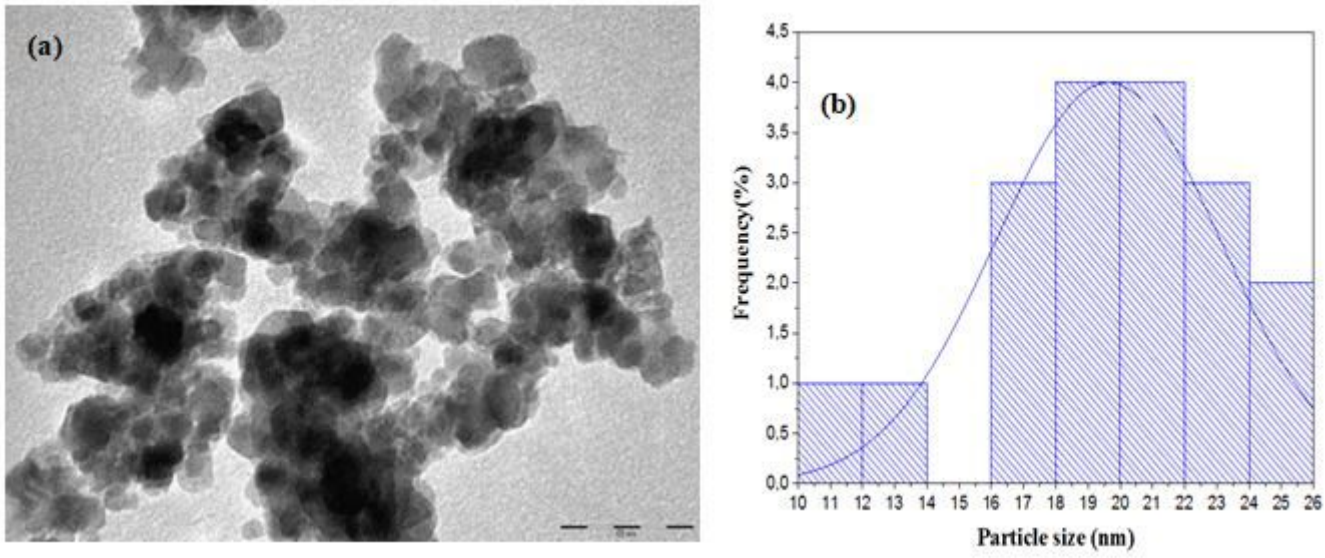

Figure 5

The TEM analysis and particles size distribution of the nanoparticle ZnFe_1.98 □□Gd□_0.01 Sm□_0.01 O_4

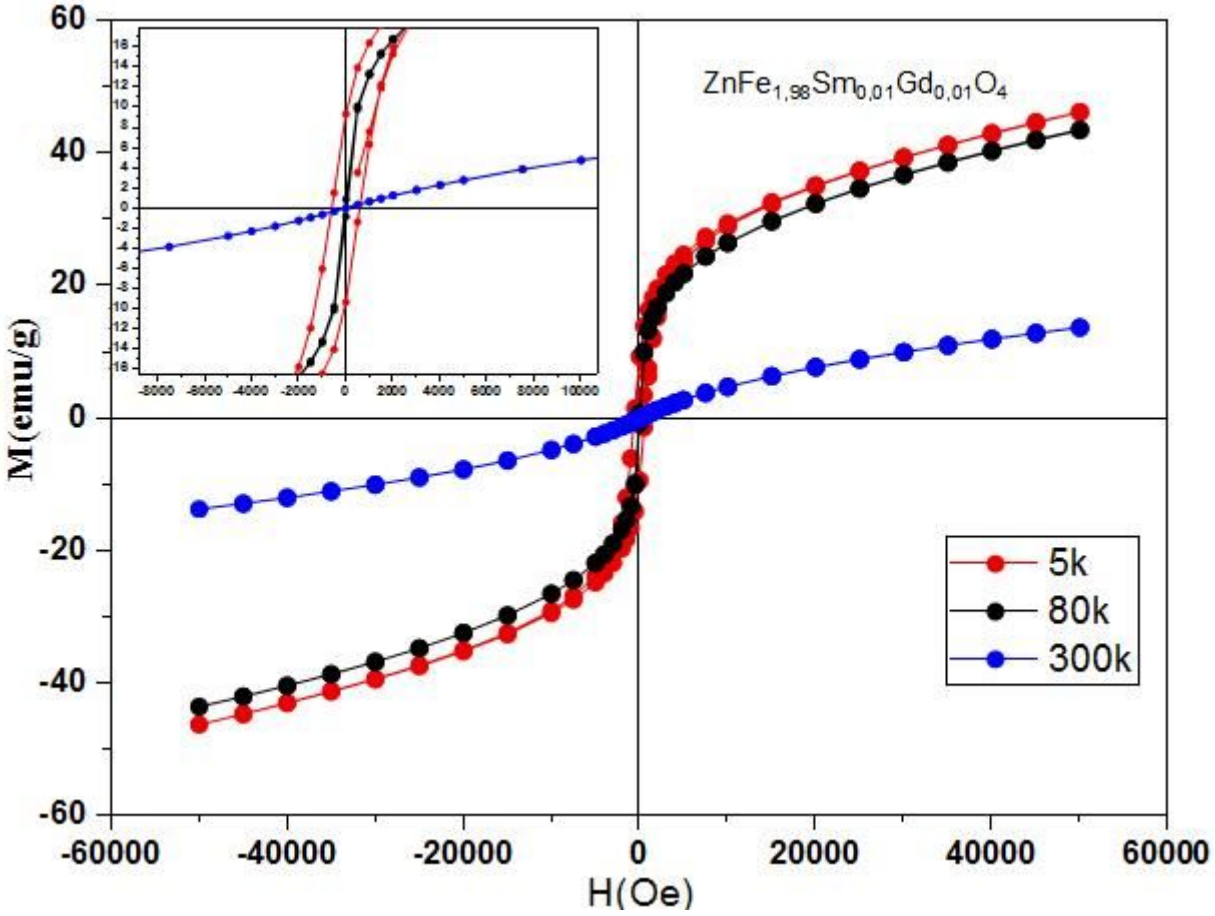

Figure 6

Hysteresis loops of sample ZnFe_1.98 □□Gd□_0.01 Sm□_0.01 O_4

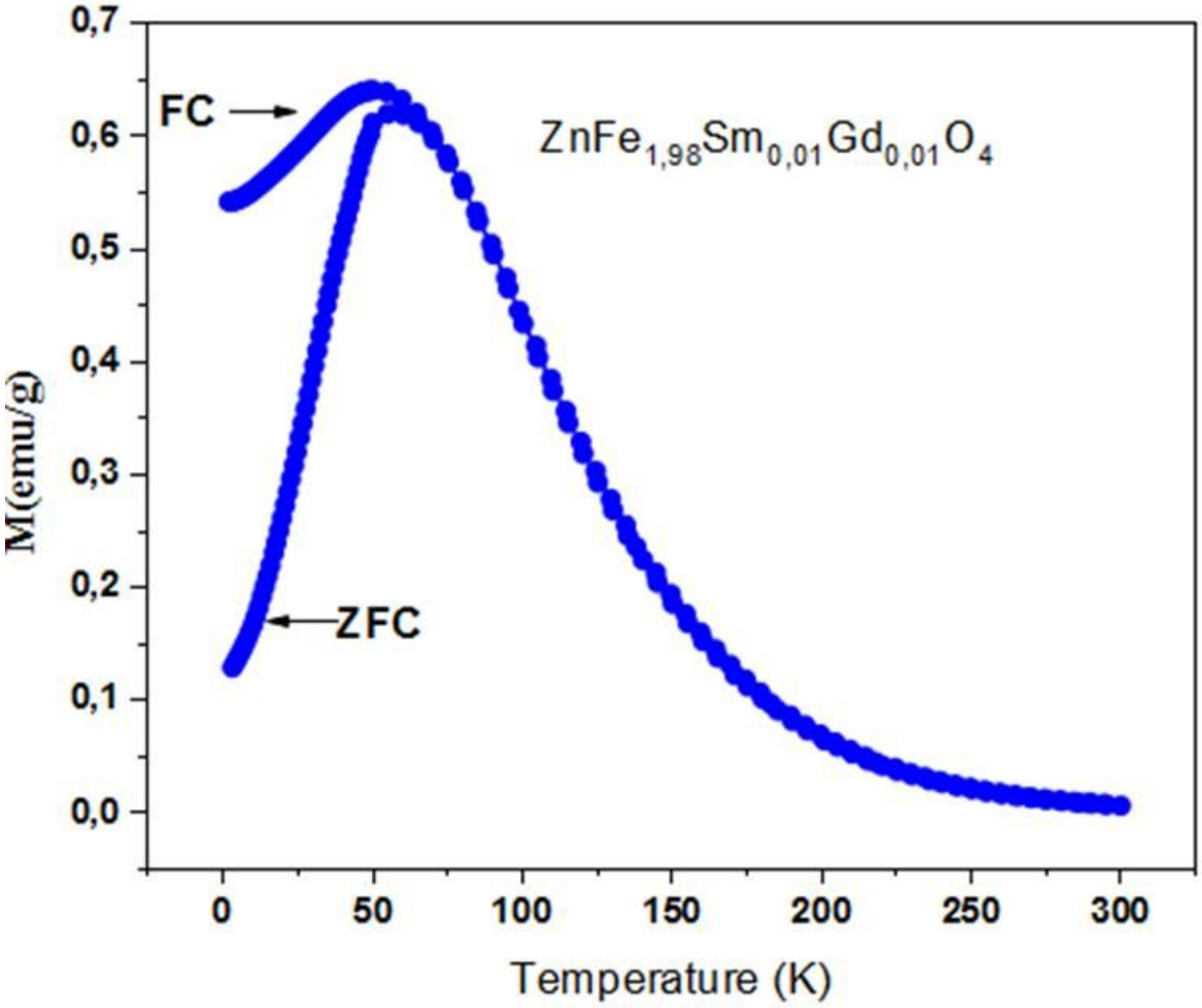

Figure 7

Zero field cooled and field cooled magnetization vs. temperature recorded in an external field of 100 Oe